Error Growth Dynamics within Convection-Allowing Ensemble Forecasts over Central U.S. Regions for Days of Active Convection

Xiaoran Zhuang[1,2,3], Ming Xue[2], Jinzhong Min[3], Zhiming Kang[1], Naigeng Wu[3,4], and Fanyou Kong[2]

[1]Jiangsu Meteorological Observatory, Jiangsu Meteorological Bureau, Nanjing 210008, China
[2] School of Meteorology and Center for Analysis and Prediction of Storms, University of Oklahoma
[3] Collaborative Innovation Center on Forecast and Evaluation of Meteorological Disasters, Key Laboratory of Meteorological Disaster of Education, Nanjing University of Information Science and Technology, Nanjing, China
[4] Key Laboratory of Regional Numerical Weather Prediction, Institute of Tropical and Marine Meteorology, China Meteorological Administration, Guangzhou, China

Submitted to Monthly Weather Review
August 2020

Corresponding author:
Ming Xue (mxue@ou.edu)
Center for Analysis and Prediction of Storms, University of Oklahoma, Norman OK 73072

Abstract

Error growth is investigated based on convection-allowing ensemble forecasts starting from 0000 UTC for 14 active convection events over central to eastern U.S. regions from spring 2018. The analysis domain is divided into the NW, NE, SE and SW quadrants (subregions). Total difference energy and its decompositions are used to measure and analyze error growth at and across scales. Special attention is paid to the dominant types of convection with respect to their forcing mechanisms in the four subregions and the associated difference in precipitation diurnal cycles. The discussions on the average behaviors of error growth in each region are supplemented by 4 representative cases. Results show that the meso-γ-scale error growth is directly linked to precipitation diurnal cycle while meso-α-scale error growth has strong link to large scale forcing. Upscale error growth is evident in all regions/cases but up-amplitude growth within own scale plays different roles in different regions/cases.

When large-scale flow is important (as in the NE region), precipitation is strongly modulated by the large-scale forcing and becomes more organized with time, and upscale transfer of forecast error is stronger. On the other hand, when local instability plays more dominant roles (as in the SE region), precipitation is overall least organized and has the weakest diurnal variations. Its associated errors at the $\gamma-$ and β-scale can reach their peaks sooner and meso-α-scale error tends to rely more on growth of error with its own scale. Small-scale forecast errors are directly impacted by convective activities and have short response time to convection while increasingly larger scale errors have longer response times and delayed phase within the diurnal cycle.

1. Introduction

Convective events frequently occur over central U.S. in the spring season and the associated flooding can produce significant threats to life and properties (Ashley and Ashley 2008). Recent studies revealed that convection-allowing numerical prediction models have advantages over coarser-resolution models in representing convective modes and diurnal cycle of precipitation (e.g. Clark et al. 2007), but the forecast skill does not always improve as model resolution increases (Lean et al. 2008; Mass et al. 2002; Walser et al. 2004). On the other hand, forecast skill often decreases fast with forecast range due to rapid forecast error growth (Kain et al. 2010; Surcel et al. 2015). These issues speak to the need for better understanding the predictability of convective events, and associated error growth across scales (Sun and Zhang 2016; Zhuang et al. 2020).

Understanding forecast error growth is a fundamental issue within the realm of predictability (Fritsch and Carbone 2004; Hohenegger and Schar 2007; Johnson et al. 2013; Kong et al. 2006), and related research issues include the growth of errors at different scales and their interactions (Bachmann et al. 2019; Bierdel et al. 2017), and the predictability limitation estimation (Judt et al. 2016; Walser et al. 2004). Through the study of error growth dynamics within a highly idealized model, Lorenz (1969) revealed important scale interactions pertaining to atmospheric predictability. Studies in more realistic settings have shown that very small amplitude and small-scale initial errors can grow upscale and contaminate mesoscale and large-scale processes (Hohenegger et al. 2006; Tan et al. 2004; Zhang et al. 2003). Zhang et al. (2007) proposed a three-stage error growth conceptual model using an idealized baroclinic wave model. This conceptual model suggests that the intrinsic predictability at larger scales is limited by upscale transfer of smaller scale errors: Stage 1 encompasses fast increase and an early saturation of small-scale errors that are confined to precipitation regions in presence of convective instability and latent heat release; Stage 2 corresponds to the transition stage when small-scale errors begin to spread from the precipitation regions and project to balanced motions through geostrophic adjustment processes (Bierdel et al.

2017). After that, errors continue to grow through background baroclinic instability at a slower rate in Stage 3. The model has been subsequently applied to investigating and explaining error growth dynamics in both idealized and more realistic modeling studies (Selz and Craig 2015; Sun and Zhang 2016; Zhang 2019). On the contrary, initial errors at larger scales have been reported by other authors to account for much of the error growth and for controlling forecast accuracy regardless of the presence of small scale errors (Durran and Gingrich 2014; Durran and Weyn 2015; Weyn and Durran 2017, 2018, 2019).

Another important question concerning error growth is what mechanism determines the diurnal aspect of error growth (Keil et al. 2014; Klasa et al. 2018; Nielsen and Schumacher 2016; Wu et al. 2020; Zhang et al. 2007). In general, the baroclinic instability associated with horizontal temperature gradients and the convective instability associated with unstable vertical profiles for moist convection are considered as the two main driving mechanisms for forecast error growth at the large and small scales, respectively (Bei and Zhang 2014; Nielsen and Schumacher 2016; Zhang et al. 2007). Zhang et al. (2007) found that moist convection is not only important in initiating error, but also in maintaining subsequent error growth at small scales. Weyn and Durran (2017) showed that the forecast error also exhibits up-amplitude growth in addition to upscale growth. Nielsen and Schumacher (2016) concluded that the forecast error evolution can be decomposed into a steadily growing mode that determines the amplitude increase, and a superimposed mode dominated by strong moist convection activities (e.g., those associated with solar-forced diurnal precipitation peak) that determine the "shape" of error growth curve. However, since convective events are inherently scale sensitive, it is important to understand characteristics of error growth across scales.

Previous studies also reported that the predictability of convective events depends on the impact of large-scale forcing on convection, and the convective events are often categorized into different regimes, namely, those that are strongly forced and weakly forced. As reported by Keil et al. (2014), in case of strongly forced convection, large-scale flow dominates error growth, while for weakly

98 forced convection controlled by local instabilities the contributions from both sources are
99 approximately equal. Nielsen and Schumacher (2016) also found that in a case with strong convective
100 to synoptic-scale interactions the forecast error can continuously increase. By investigating error
101 evolution under different convective regimes, Klasa et al. (2019) also indicated through case studies
102 that large-scale flow and diurnal solar forcing together determine the overall evolution of error
103 growth.

104 During the spring of the central U.S. regions, convective systems are often active with multiscale
105 interactions (Carbone and Tuttle 2008; Carbone et al. 2002b; Dai et al. 1999; Knievel et al. 2004;
106 Surcel et al. 2010; Trier et al. 2006); it is common for initially more isolated storm cells to organize
107 into mesoscale convective systems (MCSs) in the region. In this study, we investigate scale-dependent
108 error growth for 13 convective events during May 2018 with convection-allowing model (CAM)
109 ensemble forecasts at 3 km grid spacing covering the contiguous United States (CONUS). The large
110 convection-allowing grid allows for the representation of scales from meso-γ through meso-α scales.
111 We will focus on the forecast error analyses in a domain that covers the central Plains east of the
112 Rockies through the mid-west and much of the southeast regions, sampling convection of different
113 types. The study period spans early spring (when large-scale forcing is more prevalent) to late spring
114 (when locally forced convection is more prevalent) (Surcel et al. 2015; Surcel et al. 2017), allowing for
115 a diverse collection of different convection types and forcing mechanisms that regulate error growth
116 dynamics within CAM forecasts. We use the total difference energy within the forecast ensemble and
117 the scale decompositions of the difference energy as the proxy to measure error growth at and across
118 scales. So far, studies examining growth of errors across scales and within their scales with large
119 continent-sized CAM models, and how the error growth depends on the type of convection and the
120 degree of synoptic scale forcing are few and limited (e.g., Surcel et al. 2015; Surcel et al. 2017), and
121 some of the existing studies are based on individual case studies (e.g., Flack et al. 2017; Wapler et al.
122 2015). More studies on these issues are needed.

As the main goals, this study is to answer the following questions: 1) What are the general characteristics of precipitation and associated error growth with respect to different convection types and forcing mechanisms; 2) What are the characteristics of error growth in terms of different spatial scales and in regions dominated by different convection types; 3) What mechanisms dominate the diurnal evolution of forecast error. These goals provide insights into the predictability of convective events across the central U.S. regions within CAM forecasts, and potentially aid the optimal design of CAM ensemble forecast systems and provide guidance to ensemble data assimilation and forecast model improvement. For example, a better understanding of the relative impact of initial condition perturbations at different scales on ensemble variances across the scales within the forecasts of different ranges, and how the impact depends on weather regimes can provide guidance on where attention should be focused when creating initial condition perturbations for CAM ensemble forecasting systems of limited size and the best method to use for creating such perturbations

The rest of this study is organized as follows. The datasets employed in this study are introduced in section 2. Section 3 to section 5 discuss the general characteristics of precipitation systems and error growth, and the error growth mechanisms, and section 6 discusses four specific cases in more detail. Conclusions and further discussions are given in section 7.

2. Data and methods

a. Forecasts from the CAPS HWT Spring Forecast Experiment Ensemble

The Spring Forecast Experiments have been organized by the NOAA Hazardous Weather Testbed (HWT, http://hwt.nssl.noaa.gov/spring_experiment) every spring since 2007, and the Center for the Analysis and Prediction of Storms (CAPS) has been contributing the largest number of CAM ensemble forecasts every year until recently (e.g., Clark et al. 2009; Clark et al. 2018; Xue et al. 2007). In 2018, most ensemble forecasts produced by CAPS used the Advanced Weather Research and Forecasting (WRF-ARW) Model (Skamarock et al. 2008). Similar to experiments described in Clark et al. (2018) for

2016 Forecast Experiments, the CAPS CAM ensemble forecasts of 2018 included several sets, one included initial condition (IC)/lateral boundary condition (LBC) perturbations as well as different physics parameterizations, and one included IC and LBC perturbations only (i.e., all members used the same physics). The third set used stochastic perturbations based on a single suite of physics instead of multiple physics. In this study, the set using the same physics is used given our focus on IC error growth. The physics package includes the Thompson microphysics (Thompson et al. 2008), Noah land surface model (Mitchell 2005), and MYJ planetary boundary layer (Janić 2001) scheme. The Stage-IV precipitation product (Lin and Mitchell 2005) is employed as the observed precipitation data for verification purpose and we focus on the first 24 hours of forecast.

The IC of the control member of ensemble was produced by assimilating radar (reflectivity and velocity) and conventional (surface observations and radiosondes) data using the ARPS 3DVar data assimilation system (Xue et al. 2003) together with its cloud analysis package (Hu et al. 2006a; Hu et al. 2006b), using the 0000 UTC 12-km North American Mesoscale Forecast System (NAM) model analysis at the background. The 3 hourly NAM forecasts are used as the LBCs. The perturbed ICs and LBCs for other ensemble members are generated by adding perturbations derived from the 2100 UTC cycle forecasts of the operational short-range ensemble forecast (SREF) system of NCEP (Du et al. 2009) to the IC and LBC of the control member. All forecasts are initialized at 0000 UTC (1800 CST) on weekdays with a forecast range to 60 h, on the 3-km grid spacing CONUS grid (see Fig. 1). Previous studies on similarly configured forecasts produced by CAPS have reported that diurnal cycles of precipitation over central U.S. regions can be reasonably reproduced by the forecasts (Berenguer et al. 2012; Surcel et al. 2010; Surcel et al. 2015; Surcel et al. 2017). The radar data assimilation significantly alleviates the precipitation spinup problem (Kain et al. 2010; Skinner et al. 2020). Twenty-four-hour forecasts from 14 days of the CAPS ensemble forecasts from May 2018 that have active convection starting at the initial condition time (0000 UTC) are chosen to analyze IC error growth in this study.

b. Representation of forecast error

Following Nielsen and Schumacher (2016), the Root Mean Difference Total Energy (RMDTE) is used to represent forecast error, in which the horizontal DTE (Zhang et al. 2003) as a function of the grid point and time can be defined as

$$\mathrm{DTE}(\lambda)_{i,j,t} = \frac{1}{N}\sum_{n=1}^{N}\sum_{k=0}^{K}\frac{p(k+1)-p(k)}{p(0)}\frac{1}{2}\left[u(\lambda)'_{i,j,k,t,n}{}^{2} + v(\lambda)'_{i,j,k,t,n}{}^{2} + \frac{C_p}{T_r}\left(T(\lambda)'_{i,j,k,t,n}\right)^2\right], \quad (1)$$

where u', v', and T' are respectively the differences of zonal wind, meridional wind, and temperature from the ensemble mean. $C_p = 1004.9\ \mathrm{J\,kg^{-1}K^{-1}}$ is the heat capacity of dry air at constant pressure and $T_r = 270\ \mathrm{K}$ is a reference temperature. N is the number of ensemble members, the subscripts *i*, *j*, *k*, *t*, *n,* and λ represent the grid indices in *x*, *y*, and vertical directions, forecast time level, ensemble member, and spatial scale, respectively. The k index covers vertical layers from 925 to 500 hPa where most precipitation systems occur. *p* denotes the pressure of each vertical layer.

Since RMDTE values vary significantly across the convective events, we use the normalized RMDTE (NRMDTE) to reduce variations across convective events following Nielsen and Schumacher (2016). The NRMDTE is defined as the ratio of RMDTE to total mean kinetic energy (TMKE), and TMKE is given as

$$TMKE_{i,j,t} = \sum_{k=0}^{K}\frac{p(k+1)-p(k)}{p(0)}\left(\frac{1}{N}\sum_{n=1}^{N}\frac{1}{2}\left[\bar{u}^2_{i,j,k,t,n} + \bar{v}^2_{i,j,k,t,n}\right]\right), \quad (2)$$

where overbar denotes ensemble mean. Then NRMDTE can be computed

$$NRMDTE(\lambda)_{i,j,t} = \sqrt{\frac{DTE(\lambda)_{i,j,t}}{TMKE_{i,j,t}}}. \quad (3)$$

In Eq. (2), the temperature term is excluded from Eq. (1) to allow the TMKE to dominantly vary with the convective situation in question rather than with latitudinal variation in temperature (Nielsen and Schumacher 2016). Based on the above, the evolution of forecast error (as measured in a form of ensemble perturbations) can be quantitatively assessed by calculating NRMDTE over time, which can also be used to measure practical predictability. In general, the predictability within ensemble

forecasts for a convective case is destroyed when there is large increase in NRMDTE (Judt et al. 2016). In summary, RMDTE provides a measure of the magnitude of forecast errors and is applicable to individual cases while NRMDTE does not measure the absolute magnitude but assesses the mean behaviors of forecast error growth for a group of cases and informs predictability. In section 3, we employ NRMDTE to understand the mean error growth dynamics over all 14 cases, while in sections 5 and 6, RMDTE is used for correlation analysis and case studies.

c. Analysis domain and case selection

The analyses of the CAM forecasts and observations are carried out over the central U.S. region with four subregions as illustrated in Fig. 1. The overall analysis region is between the Rocky Mountains and Appalachian Mountains, which is further divided into four quadrants with equal size to allow for examination of precipitation diversity in the NW, NE, SE, and SW regions. Twenty-four-hour forecasts from 13 days of May 2018 that have active convection at the IC time are chosen from the CAPS ensemble forecasts to analyze IC error growth in this study (see Fig. 2 for a list of dates). All forecasts start at 0000 UTC. With radar data assimilated into the ICs containing active convection, errors at all scales are expected to grow from the beginning.

3. The general characteristics of precipitation systems in the forecasts

a. Mean synoptic overview

Figure 2 gives the temporal evolution of convective available potential energy (CAPE) computed from the control forecast averaged over the entire analysis domain for each of the 14 cases. The CAPE values show clear diurnal cycles with steep increases after 12 h (0600 CST) due to daytime solar heating and they reach maximum at around 20 h (1400 LST). Specifically, cases during late May show more pronounced diurnal variations and higher CAPE values than early May cases. This is consistent with previous studies (Dai et al. 1999; Surcel et al. 2015), in which early spring CAPE is affected more by large scale circulations while late spring CAPE is more controlled by diurnal cycle due to solar heating. In the horizontal plane view (Fig. 3), the CAPE averaged over all cases is mainly concentrated

in the southern part of the analysis domain that is associated with a strong mean 925-hPa low-level jet (LLJ) originated from the Gulf coast. Diurnal characteristics consistent with the boundary layer LLJs predicted by the inertial oscillation theory of Blackadar (1957) are found with the LLJ; it strengthens during the nocturnal time (Fig. 3a-d) and weakens during the day with the development of boundary layer vertical mixing (Fig. 3e-h). The enhanced nocturnal LLJ transports more moisture into the central Great Plains and also produces low-level convergence at its northern terminus that promotes organized convection (Carbone and Tuttle 2008; Trier et al. 2017).

b. Classification of precipitation types

Figure 4 displays the spatial distributions of total frequency (number of times across the 14 days) of 1-h precipitation exceeding 0.5 mm h^{-1} with different ending times. In general, there are four primary modes of precipitation that are linked to different forcing mechanisms over the analysis domain. The main precipitation in the NW quadrant is found near the western boundary of the region at 0300 and 0600 UTC (Fig. 4a,b), which is mostly from convective systems that originated in the afternoon over the Rocky Range in central Colorado and moved eastward into the region (Carbone et al. 2002a; Sun et al. 2016; Surcel et al. 2010). By 0900 and 1200 UTC (Fig. 4c, d), the precipitation is mainly found in central and eastern Nebraska, along a zone that extends eastward into the NE quadrant. This zone is associated with a quasi-stationary front that forms between the generally southerly flows from the Gulf and the higher latitude air mass (see Fig. 3). The zone is also the northern terminus of the boundary layer LLJ where low level convergence is strong and prone to trigger night time convection when the LLJ jet is enhanced (Savijarvi 1991; Trier et al. 2017). The precipitation in Nebraska between 0600 and 1200 UTC should be the combined result of eastward propagation of afternoon convection from the Rockies and those that develop at the northern terminus of the nocturnal LLJ. The convection in the northern part of the NE quadrant is mainly found at the quasi-stationary front, and it weakens by 1500 UTC (Fig. 4e) and mostly disappears by 1800 UTC or close to noon local time. The latter should be related to the weakening of the southerly flows

247 associated with the boundary layer LLJ as daytime boundary layer mixing slows down the flows
248 (Blackadar 1957; Xue et al. 2018). The quasi-stationary front is in a sense analogous to the Mei-yu
249 front found over eastern Asia in late spring to early summer (Chen et al. 2018).

250 In the southern quadrants, the direct effects of the diurnal changes in solar heating is strong,
251 and convection tends to be strongest in the afternoon into early evening. In the SW quadrant (Fig.
252 4e), precipitation is most prominent in the Texas panhandle region in a north-south zone that is
253 associated with a quasi-stationary dryline that frequently triggers convection in the late afternoon in
254 the spring (Liu and Xue 2008; Schaefer 1986; Xue and Martin 2006). The convective storms initiated
255 along the dryline often move eastward across the southern Great Plains and organize into quasi-
256 linear convective systems or squall lines in the process. In the SE quadrant, we observe mostly small-
257 scale and scattered popcorn-type convection in the daytime, especially in the afternoon and early
258 evening (Figs. 4a, g, h), some along the Gulf Coast. These cells form due to solar heating and
259 associated land/see-breeze circulations (Berenguer et al. 2012; Surcel et al. 2010). Given that the
260 precipitation in the four quadrants or sub-regions appears to be dominated by convective systems of
261 mostly different origins and forcing mechanisms, many of our subsequent discussions will be focused
262 on the four subregions, and we will investigate and contrast the precipitation diurnal cycles and
263 associated characteristics of error growth for the respective regions.

264 *c. Mean diurnal cycles of precipitation*

265 Figure 5 shows the subdomain-averaged hourly precipitation over 24 hours for the 14 forecasts
266 and their mean, and the corresponding observations. The observed precipitation rates show different
267 diurnal features for different subregions. As discussed earlier, the NW region that is mainly affected
268 by propagating convective systems coming from the Rockies and somewhat by convection forced by
269 nocturnal LLJ, the peak precipitation is found around 0000 UTC (1800 CST, Fig. 5a). The rate decreases
270 steadily into the evening and reaches minimum at around 1600 UTC (1000 CST). The precipitation
271 starts to pick up significantly in early afternoon (~2000 UTC or 1400 CST) and increase to the second

day peak at 0000 UTC. In the NE region (Fig. 5b), the precipitation peaks at 0600 UTC or around mid-night, consistent with the fact that nocturnal LLJ forcing plays the largest role in that region in this season (Dai et al. 1999). The minimum is around 1700 UTC. For the SW region, precipitation mostly occurs in the local afternoon after 1700 UTC (noon EST) and before 0200 UTC, and the maximum occurs at around 2100 UTC, due to the predominant effect of solar heating (Fig. 5d). For the SW region, precipitation peaks around 0000 UTC or 1800 CST, due to frequent initiation of convection along the dryline in western Texas in late afternoon, and subsequent eastward propagation. These observed diurnal characteristics are reasonably well reproduced by the model (cf. black dashed and solid lines in Fig. 5) although there are magnitude errors. For the individual cases, several of them had rather weak precipitation throughout the 24 hours. For those that have significant amount of precipitation, the general diurnal trends mostly match the mean observation. The cases with more precipitation are often associated with favorable synoptic scale flow patterns and related forcing.

Overall, the northern regions tend to be more affected by synoptic scale circulations (cyclones) in May (especially for the NE region), and at the low levels by convergence induced by nighttime LLJ. For the southern regions, synoptic scale forcing tends to be weaker, and boundary layer thermal forcing dominates, especially in the SE region. In the SW region, dryline dynamics play additional roles. The fact that the mean precipitation diurnal cycles are reproduced reasonably well in the model suggest that the forecasts can be used to investigate diurnal cycle-dependent forecast error growth. It is noted that the time-averaged forecast precipitation rates in the subdomains all show significant precipitation (NW: 0.23, NE: 0.25, SW: 0.15, SE: 0.21 mm h^{-1}).

4. Characteristics of error growth in forecasts

a. Spatiotemporal characteristics of total error growth

Previous studies have revealed a strong relationship between error (energy) growth and precipitation (Flack et al. 2017; Johnson et al. 2013; Nielsen and Schumacher 2016; Wu et al. 2020). Given the strong zonal propagation of convection (Surcel et al. 2010 and Fig. 4), we first analyze the

297 mean error growth and associated precipitation rate in time-longitude coordinates in terms of
298 Hovmoller diagrams (for the northern and southern half of the domain with averaging over the
299 latitudinal range of the half domains). Figure 6 shows the time-longitude Hovmoller diagrams of the
300 total NRMDTE and corresponding precipitation rates averaged over all 14 cases, plotted for the
301 northern (Fig. 6a) and southern half of the overall domain (Fig. 6b).

302 In the northern half domain (combination of NW and NE subdomains), the total NRMDTE
303 corresponds well with the two progressive precipitation systems (Fig. 6a): the orographically forced
304 precipitation systems coming out the Rockies in the afternoon propagating through the NW region
305 (indicated by the long gray arrow labeled NW) and the nocturnally forced precipitation systems
306 forming in the north-central part along the quasi-stationary front that propagate eastward and
307 dissipate in the morning hours in the NE subdomain (the gray arrow labeled NE, and see also Fig. 4a-
308 d). West of 100° W, the NRMDTE grows quickly, reaching over 0.3 after ~3 h (Fig. 6a), the region of
309 large NRMDTE spreads downstream in a fan pattern, with the largest values more or less tracking the
310 maximum precipitation 'ridge' in the Hovmoller diagram while lagging in time in terms of the 'ridge
311 line' by a couple of hours. Corresponding to the precipitation initiated along the quasi-stationary
312 front near and east of 96° W and sustaining through the night while propagating eastward (along the
313 arrow labeled NE), errors develop more or less following the precipitation track in the Hovmoller
314 diagram and expand in east-west extent. The two regions of NRMDTE > 0.31 (red shadings) merge
315 together after 10 h, and occupy the zone between 88° and 104° W through 24 hours, with the
316 expanding region of high NRMDTE (gray color) being mostly associated with western propagating
317 band of precipitation. These results clearly show that the NRMDTE growth is strongly tied to the
318 development and decay, and propagation of convective systems which exhibit clear diurnal cycles.
319 For the eastern band, NRMDTE decreases after 16 h when the precipitation intensity decreases in the
320 late morning hours. The western band has larger NRMDTE values, indicating greater uncertainties
321 and lower predictability with these precipitation systems in the NW domain.

For the southern part of the overall domain (Fig. 6b), there are clearly two branches of larger NRMDTE values, corresponding to the eastward propagating dryline-initiated precipitation systems in the SW region and the local thermally forced precipitation systems in the SE region. The NRMDTE associated with the thermally forced convection in SE clearly develops much faster and the gray color fills much of the domain after 10 hours, indicating low predictability with such often-disorganized thermal convection that is mainly active in the afternoon through mid-night hours. The error remains larger in the morning hours though, indicating the effects of widespread afternoon convection that also cause upscale error growth (Hohenegger et al. 2006). In comparison, errors associated with the convection in the SW region grow much slower and gain lower values; this may be partly because the dryline-initiated convection tends to become organized when they propagate through the southern Great Plains, where the boundary layer tends to be capped by an inversion layer to prevent widespread convection. The decay of convection from late morning also limited further error growth (Fig. 6b).

The above results indicate that forecast error growth within a CAM ensemble often closely follows the precipitation systems and the errors tend to grow upscale from the precipitation regions, and the behaviors of error growth are highly dependent on the characteristics of the precipitation systems, including their primary forcing mechanism, propagation and organization.

Figure 7a shows the temporal evolution of total NRMDTE averaged over all 14 cases for the entire analysis domain and each of the subdomains, respectively. Diurnal variations in the NRMDTE over the entire domain (black dashed curve) similar to that found in Nielsen and Schumacher (2016) are observed, with growth mainly found in the first ~12 h and last ~5 h of the 24 h forecasts, corresponding to the evening through early morning hours, and the afternoon hours. NRMDTE remains level after sunrise through noon due to suppression of much of the convection. The total NRMDTEs for different subregions exhibit different magnitudes and trends. The NRMDTE for the SE region is the largest from the beginning (indicating larger uncertainties in its IC) and continues to

grow throughout the 24 hours, and grows the fastest in the afternoon and early evening, not surprisingly. The NRMDTE in the NW region is the second largest, and goes through growth, decay and growth cycles, with the decay between 1000 and 1400 CST being the most evident. Given the faster error growth, the predictability of convection in these two regions is lower (Judt et al. 2016; Nielsen and Schumacher 2016). In comparison, convective systems in the SW and NE regions have lower errors and generally similar diurnal variations. These systems have higher predictability due to stronger control of synoptic and mesoscale environments that are associated with dryline and quasi-stationary frontal circulations, respectively.

b. Spatiotemporal characteristics of error growth at different scales

To further understand the error growth dynamics, the NRMDTEs at and across different scales are assessed. The discrete cosine transform (DCT) (Denis et al. 2002; Surcel et al. 2014; Zhuang et al. 2020) is employed to decompose the dynamic variables into three scales, i.e., the meso-γ, meso-β, meso-α scales (the longest resolved wavelength for the analysis domain is 3720 km or twice the east-west width of the domain), with the dividing wavelengths being 20 and 200 km between them. In this paper, we refer to these scales as convective scale, mesoscale and synoptic or large-scale, or as γ, β, and α scales for brevity. NRMDTEs are then calculated for these three scales.

As shown in Figs. 7b-7d, the scale-dependent error growth for each subregion exhibits a "stepwise" feature, i.e., the NRMDTEs increase with increasing spatial scales at lagging times, reaching their peaks at successively later hours as the scale increases, indicative of upscale transfer of errors (Selz and Craig 2015; Zhang et al. 2007). At the first stage, the γ-scale NRMDTEs rapidly increase in the precipitation regions and reach peak between 2 (SE) and 5 h (NW) (Fig. 7b and Figs. 8a, d). The γ-scale errors at the initial time are very low because convection was introduced into the IC using the deterministic cloud analysis of radar observations (without convective scale perturbations) while the SREF-derived IC perturbations span only mesoscales and up (Johnson et al. 2013).

372 The errors at the β-scale increase rapidly in the first ~3 hours, then continue to grow through ~8
373 hours and spread beyond the precipitation regions (Fig. 7c and Figs. 8b, 8e); this may be partly
374 attributed to the slower error growth at longer wavelengths (Lorenz 1969) and partly to the upscale
375 transfer of errors from γ scale (Selz and Craig 2015; Sun and Zhang 2016). After the peak error is
376 reached, the error decreases noticeably in most of the subregions (Fig. 7c), and such decreases
377 correspond closely to the weakening of precipitation as shown in the Hovmoller diagrams (Fig. 8b, e).
378 The growth picks up again (Fig. 7c) when precipitation redevelops after 18 h (Fig. 8b, e), indicating
379 the direct contribution of moist convection to mesoscale error growth, as emphasized by Zhang et al.
380 (2007).

381 At the α scale, the NRMDTE starts at relatively high levels, which comes from the initial
382 perturbations derived from SREF 3-hour forecasts. The NRMDTE at initial time is the highest in the SE
383 subdomain mainly because the ensemble mean total energy used to do normalization is lower in this
384 weakly forced region (see Fig. 14a later for an individual case for the region). Compared to other
385 regions, the diurnal variations of precipitation in SE region are weaker and there is much less east-
386 west propagation (Fig. 8f), and its NRMDTE is able to grow monotonically throughout the 24 hours
387 (green curve in Fig. 7d).

388 The α-scale NRMDTE in other three subregions grows slowly in the first 3-4 h (Fig. 7d), then goes
389 into a stage of fast growth before levelling off at 10-12 h. The NRMDTE decreases somewhat
390 afterwards then starts to grow again at 20 h (Fig. 7d) when precipitation redevelops again in the
391 afternoon (Figs. 8f). The apparent connection of α-scale NRMDTE to the diurnal cycles of precipitation,
392 and the delayed phase of error growth compared to those at γ and β scales clearly indicates significant
393 upscale error growth feeding off moist convection in these regions.

394 Overall, similar to the precipitation rate (Fig. 5), errors in the γ scales (Fig. 7b) exhibit pronounced
395 diurnal cycles given their direct link and fast response to convective activities. The errors at these
396 scales usually decay when convection die out. For errors at the β and α scales, the diurnal responses

are weaker and the peaks are delayed, due to their slower growth. Given the clear importance of precipitation or moist convection, and based on the sequence of error growth in terms of the timing of peak error, as well as the time evolution of the spatial scales of errors in the Hovmoller diagrams, we think there is clearly upscale error growth from the convective (γ) scale through the mesoscale (β scale) and synoptic (α) scale. At the same time, because of the presence of significant large scale errors in the IC, effects of large scale errors on the smaller scales are also at work (Durran and Gingrich 2014; Weyn and Durran 2019); in fact, the storms initialized from radar data are the same within the ICs of all ensemble members (c.f., curves in Fig. 7b). Therefore, the error growth model in our situation appears to be: IC errors at the mesoscale and synoptic scale grow in the ensemble and create errors at the convective scale that grow the fastest. The fast-growing convective scale errors then propagate upscale. The precipitation activities strongly modulate error growth at all scales, resulting in significant diurnal cycles of error dynamics, which are also affected by the precipitation regimes (Durran and Gingrich 2014; Weyn and Durran 2019). The upscale error propagation is the weakest in weakly forced situations. These are discussed further in the next section.

5. Effects of convection intensity and large-scale forcing on forecast error

Since error growth within CAM forecasts depends on the type of convective system or precipitation type (Keil et al. 2014; Klasa et al. 2018; Nielsen and Schumacher 2016), in this section, we evaluate the impact of precipitation type on error growth with respect to the spatial scale and forecast range via a correlation analysis.

a. Relation between moist convection intensity and forecast error

The intensity of moist convection has been reported to dominate error growth at small scales during first few forecast hours in precipitation regions (Fig. 7b, Fig. 8a, d) (Hohenegger et al. 2006; Selz and Craig 2015; Zhang et al. 2007; Zhang 2019). However, the impact of moist convection intensity on error growth at longer forecast ranges, especially with different precipitation diurnal cycles, is less clear. In this subsection, the area-average precipitation rate exceeding 0.5 mm h^{-1} is

422 used as an indicator of the intensity of moist convection, RMDTE is used to represent error growth,
423 and their relationship is evaluated with a linear regression method.

424 Figure 9 shows the scatterplots between RMDTE and moist convection intensity (both variables
425 are normalized prior to calculating the regression coefficient (Reynolds et al. 2002)) at different scales
426 and over different subregions. Different colors are used to represent different forecast periods based
427 on consideration of the stages of error growth and the diurnal variability of precipitation and errors
428 at different scales: 1) the black dots represent period 1 (0-9 h, 1800-0300 LST), encompassing the fast
429 increase of γ-scale errors and their associated saturation; 2) the cold color dots indicate period 2 (10-
430 15 h, 0400-0900 LST), containing the increase and saturation of β-scale and α-scale errors; 3) the
431 warm color dots indicate period 3 (16-24 h, 1000-1800 LST) in which secondary error growth occurs
432 in the second day. Different cases are characterized by different markers. Lines in different colors
433 represent the fitting lines for different periods using linear regression.

434 Overall, the correlation between forecast error magnitude and moist convection intensity
435 increases with decreasing scales, strong positive correlations between them can be found at the γ
436 scale in all three periods (Figs. 9a1-a4). In some regions (e.g., SW), the positive relationship is even
437 stronger in period 3 (Figs. 9a4) when afternoon thermal convection is active (c.f., Fig. 7b, Fig. 8d). In
438 comparison, weak positive correlations or even negative correlations are observed at the β scale (Figs.
439 9b1-b4) and α scale at shorter forecast ranges (Figs. 9c1-c4). The correlation coefficients are generally
440 larger during periods 2 and 3 than that of period 1, even for γ scale. This result implies that the impact
441 of moist convection on error growth increases with forecast time, apparently due to the accumulative
442 effects of moist convection on forecast error.

443 Specifically, for the NW, NE, and SW regions where mesoscale to large-scale forcing linked to the
444 nocturnally strengthened LLJ during period 1 plays significant roles, the RMDTEs can be negatively
445 correlated to the strength of moist convection at the larger scales (Figs. 9b1-b3, c1-c3), and the
446 negative trend is stronger for the α scale. Weaker negative correlations are also found for the SE

447 region (Figs. b4, c4). Such negative correlation appears to be due to the delayed response of larger
448 scale errors to moist convection so that the error growth is out of phase with the convection intensity
449 time evolution. If we consider the γ-scale error shown in Fig. 7b as a proxy of moist convection
450 intensity (because of the fast response to γ-scale error to moist convection), we can see that the
451 β–scale (Fig. 7c) and α–scale (Fig. 7d) errors are increasing throughout period 1 while the γ-scale
452 errors are decreasing after 2-4 h (Fig. 7b). Such out-of-phase evolution is also evident in Fig. 8 when
453 comparing the precipitation intensity and error growth in the first 9 hours for the two larger scales.

454 In summary, moist convection impacts forecast error growth during the whole 24-h forecast
455 range. The correlation between error growth and moist convection decreases with increasing spatial
456 scale because of the increasing error response time to convection. The correlation increases with
457 forecast hours due, we believe, to the accumulative effects of convection. For the initial 8 hours of
458 forecast, the correlation is actually negative for forecast errors at the β and α scales; this is believed
459 to be related to the phase difference between the errors at these scales and smaller scale convection.

460 *b. Relationship between large-scale forcing and forecast error*

461 The impact of large-scale forcing on convection is often objectively assessed by the rate at which
462 instability is removed by convection (Keil et al. 2014). Following Done et al. (2012; 2006) and Surcel
463 et al. (2015), the convective adjustment time scale (τ_c) is introduced

464 $$\tau_c = \frac{1}{2}\frac{C_p \rho_0 T_0}{L_v g}\frac{CAPE}{p_{rate}}, \quad (4)$$

465 where C_p is the specific heat capacity of air at constant pressure, ρ_0 and T_0 are the reference density
466 and temperature, L_v is the latent heat of vaporization, *g* is the acceleration of gravity, and p_{rate} is the
467 precipitation rate. Prior to calculation, both CAPE and p_{rate} are spatially smoothed using a Gaussian
468 method with a radius of 20 km and masked with a threshold of 0.5 mm h^{-1} to avoid dry events. Lower
469 τ_c indicates a stronger degree of large-scale forcing and vice versa. In general, a threshold at the lower
470 bounds of the 3-12 hour range for τ_c could be used to distinguish strongly forced events and weakly
471 forced events (Zimmer et al. 2011), and in this study a threshold of 3 h is chosen (Keil et al. 2014). In

472 reality, as discussed in Surcel et al. (2017), there can be events in which large areas of instability are
473 consumed by convection that was initialized at the small scale and the errors grow upscale through
474 e.g., organization of small storms into larger mesoscale systems. The readers should be aware of such
475 caveats.

476 As shown in Fig. 10, τ_c has a similar diurnal cycle as CAPE with lower nighttime value (stronger
477 large-scale forcing) and higher daytime value (weaker large-scale forcing). Despite the typical use of
478 τ_c to distinguish precipitation situations, Keil et al. (2014) also suggested that τ_c could be an indicator
479 of forecast uncertainty. However, the relationship between τ_c and forecast error across and at
480 different spatial scales is still not clear.

481 Figure 11 shows the scatterplots between RMDTE and τ_c at different scales and different
482 subregions during different forecast periods. In general, the correlation coefficient is clearly
483 dependent on the forecast period. For all regions, with the initial weakening of large-scale forcing
484 (Fig. 10) with time (from nighttime to daytime), the correlation decreases correspondingly.
485 Specifically, during period 1 which is from early evening through early morning, CAPE is relatively low,
486 so that convection is more of forced type or large-scale forcing is relatively strong, we see clear
487 negative correlation between error and τ_c, especially at the two larger scales (Fig. 11b1-4, 11c1-4).
488 The correlation at the γ-scale is much weaker though still negative (Fig. 11a1-4). These results indicate
489 that the presence of larger-scale forcing is favorable for the organization of convective cells into larger
490 MCSs and for growth of errors at the two larger scales. They also suggest that the large-scale flows
491 have more control on error growth at larger scales, consistent with expectation.

492 For the longer forecast ranges in periods 2 and 3, the relationship between forecast error and
493 forcing is less clear. For the two smaller scales, the correlation for period 2 is mostly negative or close
494 to zero (for SW region), but is positive for α scale for all except NW region. This is the morning period
495 when precipitation is weakest. In period 3 when convection becomes active again, the correlation
496 becomes negative again for the two larger scales in all 4 regions (Fig. 11b1-4, 11c1-4). Therefore, the

497 relationship between large-scale forcing and forecast error growth has diurnal variations, with
498 connection to the precipitation diurnal cycle.

499 **6. Case studies**

500 In this section, four representative convective cases (A-D) primarily from the four subregions
501 with different dominant types are selected to present the forecast error growth in a more intuitive
502 manner. To simplify the description, the division of forecast range in section 5 is retained in this
503 section.

504 *a. Case A: 18 May 2018*

505 In the afternoon of 17 May 2018, convective storms formed over the Rocky Mountains in central
506 Colorado and propagated eastward into western Nebraska and South Dakota by early evening (0200
507 UTC, 18 May, Fig. 12a) and moved into central Nebraska by early morning (Fig. 12c). The associated
508 area-averaged precipitation in the NW region (black stars in Fig. 13) presents persistent decrease
509 after 4 h (2200 CST) until 17 h (1100 CST) and a subsequent daytime increase due to solar heating
510 (Fig. 12d), conforming to the mean diurnal cycle in the NW region presented in Fig. 5. These features
511 indicate that Case A is under the influence of multi-scale system interactions. The corresponding total
512 RMDTE exhibits a clear diurnal cycle with a maximum occurring at ~7 h (0100 CST) and a minimum at
513 21 h (1500 CST). At the γ scale, with the influence of strong moist convection, the RMDTE depicts
514 pronounced up-amplitude growth during the first 1 h and a slower but still significant growth until 3
515 h. The rapid growth in the first hour is partly due to the essential absence of γ-scale perturbations in
516 the ensemble ICs as mentioned earlier; the ensemble dispersion increases rapidly in response to
517 initial mesoscale and synoptic-scale perturbations derived from SREF. The RMDTE remains flat
518 between 3 and 5 h then decreases with weakening moist convection continually until 18 h (1200 CST)
519 when the error starts to increase rapidly again with the development of thermally forced afternoon
520 convection within a weak forcing environment. The β- and α-scale RMDTEs depict similar diurnal
521 cycles but with phase lag, with the peaks being reached about 4 and 9 hours later, respectively, due

to delayed response of larger-scale errors to convection. The results also indicate significant upscale transfer of convective scale error.

b. Case B: 4 May 2018

Case B is a synoptically forced convective event with a surface low pressure center moving towards northeastern U.S., producing intense precipitation in the NE subregion (black stars in Figs. 12e-h). Strong southerly low-level flows in the form of synoptic LLJ coming from the Gulf of Mexico exist around the western peripheral of the westward extending subtropical high, bringing rich moisture and energy into the mid-west region to support and maintain convection. The southerly low-level flows are further enhanced at night due to boundary layer inertial oscillation (Blackadar 1957) (Fig. 12f). It is clear that Case B is characterized by strong large-scale forcing with a pronounced lower τ_c (Fig. 13). Different from Case A in the NW region, the total RMDTE in Case B does not have the typical diurnal feature of decreased values in the morning, but shows instead double peaks at 8 h (0300 EST) and 18 h (1300 EST) (Fig. 13a); this is mostly due to the large contribution of α-scale error during the day time, which peaks at around 18 h (1300 EST). Specifically, being more of a forced type, the γ-scale RMDTE (Fig. 14b) of Case B has a slower growth rate than that of Case A and reaches peak at 5 h. Interestingly, the β-scale RMDTE reaches peak at a similar time (Fig. 13c), suggesting that organized convection dominates. During period 3, there is no secondary peak in the γ or β-scale RMDTE; this is so even though there is a significant increase in precipitation in this period. The large increase in RMDTE at the α scale in period 3 is linked to the strengthening of the low pressure system and the corresponding increase in organized frontal precipitation (Fig. 12h). As a short summary, both precipitation and error growth are dominated by evident large scale forcing in Case B, and the forecast error fits more closely to the three-stage error growth model (Zhang et al. 2007), indicative of much more prominent upscale growth of forecast error.

c. Case C: 15 May 2018

In Case C the ensemble mean fields show an eastward propagating shallow trough at the 500

547 hPa (not shown) through Texas as the convective event unfolds in the SW region (Fig. 14a-d). There
548 are moderately strong southerly to southeasterly low-level flows from the Gulf into south-central and
549 western Texas, which together with a jet aloft form strong deep-layer shear. Discrete supercells form
550 along a north-south dryline located in eastern Texas panhandle into western Oklahoma (Fig. 14a) and
551 move eastward (Figs. 14b-c) under the influence of large scale upper-level flows. The precipitation
552 diurnal cycle is broadly similar to that of Case A, in that daily precipitation maximum occurs around
553 0000 UTC (1800 CST), and the precipitation minimum occurs at around 1700 UTC (1100 CST). The
554 main difference is that Case C precipitation has a secondary maximum in the early morning (0900
555 UTC), and the precipitation throughout the morning is larger than Case A. Such early morning
556 maximum should be related to enhancement of nocturnal LLJ due to boundary layer inertial
557 oscillations, which also cause clockwise rotation of boundary layer winds (Figs. 14a, 14b) (Blackadar
558 1957; Xue et al. 2018). By the afternoon of the second day, the low-level flow is restored to the
559 southeasterly towards the panhandle areas (Fig. 14d), producing new convection along the dryline
560 (near the western edge of subregion SW, Fig. 14d).

561 The total RMDTE in Case C (red curve in Fig. 13a) has similar, strong diurnal evolution as in Case
562 A, although its peak is reached at around 9 h, 2-3 h later than in Case A (Fig. 13a). This delay is mainly
563 due to the delay in α-scale RMDTE (Fig. 13d) while the peaks of γ and β-scale RMDTE are reached at
564 essentially the same times as in Case A (Figs.13b and 13c). This is consistent with the fact that the
565 secondary precipitation peak at 0900 UTC is mainly due to forced convection at night (by nocturnal
566 LLJ-induced convergence), which have large scales and act to mainly cause growth of larger-scale
567 error that reaches its peak at ~1100 UTC. After reaching their minimum at ~1800 and ~2000 UTC,
568 respectively, the smaller-scale RMDTEs increase rapidly again as new convection develops in the
569 afternoon (Figs. 13b, 13c) but the β-scale RMDTE does not start to grow until 2200 UTC, and at a
570 slower rate. In Case C, large-scale forcing is weak in the afternoon and early evening hours (marked
571 by red circles in Fig. 13), so that the precipitation is of convective nature. The phase relations between

precipitation intensity and RMDTEs at different scales again show significant roles of upscale error propagation.

d. Case D: 16 May 2018

In Case D, the precipitation is mainly in the SE region, which is located in a zone of weak convergent flows between northerly flows from the north, and southwesterly flows on the north side of a high-pressure system over the Gulf (Figs. 14e-14h). Precipitation is from scattered convective cells that are heavier in the afternoon (16-24h) and evening hours (0-6 h) when CAPE is higher (Figs. 14h, 14e); the precipitation diurnal cycle is weaker than Cases A-C mainly because the morning precipitation minimum is at a higher level. Clearly, the precipitation in the SE region in this case is mainly associated with local thermal instability under generally favorable thermodynamic conditions with weak large-scale forcing (high τ_c; Fig. 13). Like the average NRMDTEs for all cases in the SE region (Figs. 7a, 7d), the total RMDTE and that for the α scale of Case D show almost monotonic increase throughout the 24 hours (Figs. 13a, 13d), mainly due to the monotonic increase of the α scale RMDTE. The RMDTEs for the γ and β-scales show similar diurnal variations as those for Cases C and B, except that the maximum and minimum are reached faster (Figs. 13b, 13c), suggesting less organization of scattered convective cells into mesoscale convective systems that can sustain smaller scale error growth for longer; this is consistent with the weaker large-scale forcing in this region. This behavior leads to earlier saturation of smaller scale errors and smaller amplitudes reached. The more persistent precipitation throughout the 24 hours and the weaker large-scale forcing appear to work together to produce relatively slow, but steady and monotonic growth in large-scale error in Case D (Fig. 13d).

Among the 4 cases, Cases B and D can be considered two extremes; Case B has the strongest large-scale forcing (having the least number of circles in Fig. 13), and the error growth in second half of the 24 hours is mainly dominated by large-scale flow dynamics, while Case D is dominated by disorganized thermal convection with the weakest large scale forcing (most number of green circles

in Fig. 13). In Case B, the total RMDTE continues to increase through 18 hours of forecast, in the first half mainly through rapid growth of small-scale errors and upscale transfer, and in the second half as a result of both upscale transfer and large-scale error growth in association with the large-scale dynamic system. For Case D, because of the general lack of organization of scattered convective cells into larger mesoscale convective systems, the upscale transfer of γ- and β-scale errors to α-scale is less, not enough to create a significant peak in the early morning as in other cases; the α-scale error increases mainly as a result of steady and generic growth of α-scale error itself, resulting in a monotonic curve that is less dependent on the precipitation diurnal cycle as in other cases.

7. Summary and conclusions

This study investigates the error growth dynamics of convective events over the central U.S. regions using 3-km grid spacing CAM ensemble forecasts for 14 active convection days of May 2018. The ensemble uses the same forecast model configuration among its members, and the ensemble dispersion arises purely from the IC (at 0000 UTC or 1800 CST and 1900 EST) and LBC perturbations derived from a mesoscale ensemble forecasting system. Given that the model domain covers the full CONUS, and our analysis domain is east of the Rocky Mountains and only forecasts in the first 24 hours are evaluated; since it takes some time for the upstream boundary condition to influence forecasts in the analysis domain, the IC perturbations play the primary role in ensemble dispersion (e.g., Johnson et al. 2011). In the ensemble ICs, convective-scale or γ-scale information is introduced through radar data assimilation without any perturbation. The forecast error is quantitatively characterized in terms of the (normalized) root mean difference total energy (N)RMDTE, which is used as a proxy of forecast error following earlier studies (e.g. Klasa et al. 2018; Melhauser; Zhang 2012; Nielsen; Schumacher 2016).

The analysis domain between the Rockies and the Appalachian Mountains is equally divided into the NW, NE, SE and SW subregions, and during May each subregion has its own dominant precipitation type with respect to the initiation and forcing mechanisms of convection, and hence

622 different precipitation diurnal cycles. The discussions on the average behaviors over the 14 cases in
623 each region are supplemented by 4 cases representative of precipitation in each region.
624 It is shown that when large-scale flow (synoptic scale system) is important (e.g., in the NE region),
625 the region-average precipitation is strongly modulated by the large-scale forcing, while in the SE
626 region, local thermal instability dominates and precipitation arises mostly from less organized
627 convection. Within the 24 h, the total forecast error growth approximately follows the precipitation
628 systems within Hovmoller diagrams, revealing a strong relationship between forecast error growth
629 and precipitation. Specifically, the temporal evolutions of total NRMTE for each subregion are clearly
630 linked to the precipitation diurnal cycles and convective system propagation.
631 Analyses on scale-dependent error growth show evident upscale error growth (Hohenegger and
632 Schär 2007; Selz and Craig 2015; Zhang et al. 2007) in all four regions/cases while up-amplitude
633 growth within own scale plays different roles in different regions/cases. The meso-γ-scale error
634 growth is most directly linked to precipitation diurnal cycles while meso-α-scale error growth has
635 strong link to large scale forcing. With the specific setup of the ensemble, γ-scale errors grow very
636 rapidly in the first few hours as a result of IC perturbations at β and α scales and the presence of
637 moist convection in the IC, and the first peak of γ-scale NRMDTE is reached in 2 (in SE region) to 5 (in
638 NE region) hours. The β-scale NRMDTE grows slower and reaches the first peak in 6 to 9 hours. The
639 NRMDTE at both scales decreases significantly after the first peak through early afternoon due to
640 decay/suppression of precipitation but increases rapidly again in the afternoon after the onset of new
641 afternoon convection. The α-scale NRMDTE generally follows a similar trend, but the first peak is
642 reached much later in 11 to 18 hours, clearly an indication of successively upscale transfer of errors
643 from smaller scales. In the specific example of NE precipitation case, the α-scale NRMDTE continues
644 to amplify until 18 h to a much higher level than in other cases due to the presence of an evolving
645 low-pressure system and the associated differences in strong synoptic-scale forcing. In a specific case
646 in the SE region when large systems are much less dynamic, the precipitation is least organized and

647 has weaker diurnal variations. As such, the γ– and β-scale NRMDTE peaks are reached sooner, and
648 the α-scale NRMDTE continues monotonic increase throughout the 24 hours. These results suggest
649 that for regions where large-scale forcing is weak and when convection is mostly disorganized,
650 upscale transfer of forecast error tends to be more limited and up-amplitude growth of the large-
651 scale error can be as important. For the two cases producing precipitation mainly in the SW and NW
652 regions, the convective cells tend to undergo organization into MCSs while moving eastward and
653 experiencing night-time boundary layer convergence forcing, the NRMDTEs of all three scales
654 experience growth, decay and growth cycles within the 24 h forecasts, with successive delay in the
655 phase of error evolution, indicating clear upscale error growth feeding off diurnally varying
656 convection.

657 The relationships between RMDTE and intensity of moist convection or large-scale forcing are
658 investigated based on correlation analyses for different scales and regions for different forecast
659 periods. In particular, the correlation between forecast error magnitude and moist convection
660 intensity increases with forecast hours with the forecast range due to accumulative effects of
661 convection but decreases with increasing spatial scale. At the convective scales, the correlation is
662 positive throughout the forecast period while for the β and α scales the correlation is often negative
663 during the initial period of forecast due to the delayed response of larger-scale errors to small-scale
664 convection and the resulting phase differences.

665 The effect of large-scale forcing on forecast error is also examined in terms of the correlation
666 between RMDTE and convective adjustment time scale τ_c; the forcing is considered stronger for
667 smaller τ_c. The correlation is strong and negative (positive correlation with forcing) during first 9 h at
668 the β and α scales and but much weaker at the γ scale. This implies that at a short forecast range,
669 large-scale forcing has direct positive impact on larger-scale forecast errors, while convective-scale
670 errors are controlled much less by forcing but more by thermodynamic instability. During the forecast
671 periods between 10 and 15 h, and beyond 16 h, the correlation between forecast error and forcing

672 strength is much weaker, and fluctuates around zero. This may be partly due to the specific definition
673 of the forcing degree used because convective adjustment time is usually no more than several hours.
674 For the specific case in the NE region (Case B), strong synoptic scale forcing in the second day
675 afternoon does cause large increase in large scale error.

676 Overall, the error growth dynamics on CAM forecasts in the presence of significant moist
677 convection are strongly dependent on the intensity, type and organization of precipitation, the
678 forecast period with respect to the time of day and forecast range, and the spatial scale of the error.
679 Small-scale forecast errors are directly impacted by convective activities and have short response
680 time to convection while increasingly larger scale errors have longer response times and delayed
681 phase. Within the 24 h forecasts, forecast errors generally experience growth, decay, and growth
682 cycles following the precipitation diurnal cycle. Upscale transfer of forecast error is stronger when
683 convective cells can become more organized with time which usually occur under stronger large scale
684 forcing.

685 The results of this study shed light on the predictability of spring time convective weather in
686 different regions of the U.S. and may be applicable to other parts of the world with similar flow and
687 precipitation regimes. The understanding of error growth dynamics can help guide the optimal design
688 of CAM ensemble forecasting systems. In future studies, the inclusion of meso-γ-scale perturbations
689 in the IC should also be considered and their impacts examined.

690 *Acknowledgment:* This work is jointly supported by National Key R&D Program of China
691 (2017YFC1502103), the National Natural Science Foundation of China (41905099), Natural Science
692 Foundation of Jiangsu Province(grant BK20181101), Meteorological Science Technology Innovation
693 Foundation of East China Region (grant QYHZ201802). The CAPS 2018 HWT Spring Forecast
694 Experiments forecasts were supported by NOAA Testbed Program and NWS CSTAR grant.

695

696

References

Ashley, S. T., and W. S. Ashley, 2008: Flood Fatalities in the United States. Journal of Applied Meteorology and Climatology, 47, 805-818.

Bachmann, K., C. Keil, G. C. Craig, M. Weissmann, and C. A. Welzbacher, 2019: Predictability of Deep Convection in Idealized and Operational Forecasts: Effects of Radar Data Assimilation, Orography, and Synoptic Weather Regime. Mon. Wea. Rev., 148, 63-81.

Bei, N., and F. Zhang, 2014: Mesoscale predictability of moist baroclinic waves: Variable and scale-dependent error growth. Adv. Atmos. Sci., 31, 995-1008.

Berenguer, M., M. Surcel, I. Zawadzki, M. Xue, and F. Kong, 2012: The Diurnal Cycle of Precipitation from Continental Radar Mosaics and Numerical Weather Prediction Models. Part II: Intercomparison among Numerical Models and with Nowcasting. Mon. Wea. Rev., 140, 2689-2705.

Bierdel, L., T. Selz, and G. C. Craig, 2017: Theoretical aspects of upscale error growth through the mesoscales: an analytical model. Quart. J. Roy. Meteor. Soc., 143, 3048-3059.

Blackadar, A. K., 1957: Boundary layer wind maxima and their significance for the growth of nocturnal inversions. Bull. Amer. Meteor. Soc., 38, 283-290.

Carbone, R. E., and J. D. Tuttle, 2008: Rainfall Occurrence in the U.S. Warm Season: The Diurnal Cycle. J. Climate, 21, 4132-4146.

Carbone, R. E., J. D. Tuttle, D. A. Ahijevych, and S. B. Trier, 2002a: Inferences of predictability associated with warm season precipitation episodes. J. Atmos. Sci., 59, 2033-2056.

Carbone, R. E., J. D. Tuttle, D. A. Ahijevych, and S. B. Trier, 2002b: Inferences of Predictability Associated with Warm Season Precipitation Episodes. J. Atmos. Sci., 59, 2033-2056.

Chen, X., H. Yuan, and M. Xue, 2018: Spatial spread-skill relationship in terms of agreement scales for precipitation forecasts in a convection-allowing ensemble. Quart. J. Roy. Meteor. Soc., 144, 85-98.

Clark, A. J., W. A. Gallus, and T.-C. Chen, 2007: Comparison of the Diurnal Precipitation Cycle in Convection-Resolving and Non-Convection-Resolving Mesoscale Models. Mon. Wea. Rev., 135, 3456-3473.

Clark, A. J., W. A. Gallus, Jr., M. Xue, and F. Kong, 2009: A comparison of precipitation forecast skill between small convection-permitting and large convection-parameterizing ensembles. Wea. Forecasting, 24, 1121-1140.

Clark, A. J., and Coauthors, 2018: The Community Leveraged Unified Ensemble (CLUE) in the 2016 NOAA/Hazardous

725 Weather Testbed Spring Forecasting Experiment. Bull. Am. Meteorol. Soc., 99, 1433-1448.
726 Dai, A., F. Giorgi, and K. E. Trenberth, 1999: Observed and model-simulated diurnal cycles of precipitation over the
727 contiguous United States. J. Geophys. Res. D: Atmos., 104, 6377-6402.
728 Denis, B., J. Côté, and R. Laprise, 2002: Spectral Decomposition of Two-Dimensional Atmospheric Fields on Limited-
729 Area Domains Using the Discrete Cosine Transform (DCT). Mon. Wea. Rev., 130, 1812-1829.
730 Done, J. M., G. C. Craig, S. L. Gray, and P. A. Clark, 2012: Case-to-case variability of predictability of deep convection
731 in a mesoscale model. Quart. J. Roy. Meteor. Soc., 138, 638-648.
732 Done, J. M., G. C. Craig, S. L. Gray, P. A. Clark, and M. E. B. Gray, 2006: Mesoscale simulations of organized convection:
733 Importance of convective equilibrium. Quart. J. Roy. Meteor. Soc., 132, 737-756.
734 Du, J., and Coauthors, 2009: NCEP short-range ensemble forecast (SREF) system upgrade in 2009. Preprints, 19th
735 Conf. on Numerical Weather Prediction and 23rd Conf. on Weather Analysis and Forecasting, Omaha, Nebraska,
736 Amer. Meteor. Soc. Weather and Forecasting.
737 Durran, D. R., and M. Gingrich, 2014: Atmospheric Predictability: Why Butterflies Are Not of Practical Importance. J.
738 Atmos. Sci., 71, 2476-2488.
739 Durran, D. R., and J. A. Weyn, 2015: Thunderstorms Do Not Get Butterflies. Bull. Am. Meteorol. Soc., 97, 237-243.
740 Flack, D. L. A., S. L. Gray, R. S. Plant, H. W. Lean, and G. C. Craig, 2017: Convective-Scale Perturbation Growth across
741 the Spectrum of Convective Regimes. Mon. Wea. Rev., 146, 387-405.
742 Fritsch, J. M., and R. E. Carbone, 2004: Improving Quantitative Precipitation Forecasts in the Warm Season: A USWRP
743 Research and Development Strategy. Bull. Am. Meteorol. Soc., 85, 955-966.
744 Hohenegger, C., and C. Schär, 2007: Predictability and Error Growth Dynamics in Cloud-Resolving Models. J. Atmos.
745 Sci., 64, 4467-4478.
746 Hohenegger, C., and C. Schar, 2007: Atmospheric Predictability at Synoptic Versus Cloud-Resolving Scales. Bull. Am.
747 Meteorol. Soc., 88, 1783-1794.
748 Hohenegger, C., D. Lüthi, and C. Schär, 2006: Predictability Mysteries in Cloud-Resolving Models. Mon. Wea. Rev.,
749 134, 2095-2107.
750 Hu, M., M. Xue, and K. Brewster, 2006a: 3DVAR and Cloud Analysis with WSR-88D Level-II Data for the Prediction of
751 the Fort Worth, Texas, Tornadic Thunderstorms. Part I: Cloud Analysis and Its Impact. Mon. Wea. Rev., 134, 675-
752 698.
753 Hu, M., M. Xue, J. Gao, and K. Brewster, 2006b: 3DVAR and Cloud Analysis with WSR-88D Level-II Data for the

754 Prediction of the Fort Worth, Texas, Tornadic Thunderstorms. Part II: Impact of Radial Velocity Analysis via
755 3DVAR. Mon. Wea. Rev., 134, 699-721.
756 Janić, Z. I., 2001: Nonsingular implementation of the Mellor-Yamada level 2.5 scheme in the NCEP Meso model.
757 Johnson, A., X. Wang, M. Xue, and F. Kong, 2011: Hierarchical Cluster Analysis of a Convection-Allowing Ensemble
758 during the Hazardous Weather Testbed 2009 Spring Experiment. Part II: Ensemble Clustering over the Whole
759 Experiment Period. Mon. Wea. Rev., 139, 3694-3710.
760 Johnson, A., and Coauthors, 2013: Multiscale Characteristics and Evolution of Perturbations for Warm Season
761 Convection-Allowing Precipitation Forecasts: Dependence on Background Flow and Method of Perturbation.
762 Mon. Wea. Rev., 142, 1053-1073.
763 Judt, F., S. S. Chen, and J. Berner, 2016: Predictability of tropical cyclone intensity: scale-dependent forecast error
764 growth in high-resolution stochastic kinetic-energy backscatter ensembles. Quart. J. Roy. Meteor. Soc., 142, 43-
765 57.
766 Kain, J. S., and Coauthors, 2010: Assessing advances in the assimilation of radar data within a collaborative
767 forecasting-research environment, 25, 1510-1521.
768 Keil, C., F. Heinlein, and G. C. Craig, 2014: The convective adjustment time-scale as indicator of predictability of
769 convective precipitation. Quart. J. Roy. Meteor. Soc., 140, 480-490.
770 Klasa, C., M. Arpagaus, A. Walser, and H. Wernli, 2018: On the Time Evolution of Limited-Area Ensemble Variance:
771 Case Studies with the Convection-Permitting Ensemble COSMO-E. J. Atmos. Sci., 76, 11-26.
772 Knievel, J. C., D. A. Ahijevych, and K. W. Manning, 2004: Using Temporal Modes of Rainfall to Evaluate the
773 Performance of a Numerical Weather Prediction Model. Mon. Wea. Rev., 132, 2995-3009.
774 Kong, F., K. K. Droegemeier, and N. L. Hickmon, 2006: Multiresolution Ensemble Forecasts of an Observed Tornadic
775 Thunderstorm System. Part I: Comparsion of Coarse- and Fine-Grid Experiments. Mon. Wea. Rev., 134, 807-833.
776 Lean, H. W., P. A. Clark, M. Dixon, N. M. Roberts, A. Fitch, R. Forbes, and C. Halliwell, 2008: Characteristics of High-
777 Resolution Versions of the Met Office Unified Model for Forecasting Convection over the United Kingdom. Mon.
778 Wea. Rev., 136, 3408-3424.
779 Lin, Y., and K. E. Mitchell, 2005: 1.2 the NCEP stage II/IV hourly precipitation analyses: Development and applications.
780 19th Conf. Hydrology, American Meteorological Society, San Diego, CA, USA, Citeseer.
781 Liu, H. X., and M. Xue, 2008: Prediction of convective initiation and storm evolution on 12 June 2002 during
782 IHOP_2002. Part I: Control simulation and sensitivity experiments. Mon. Wea. Rev., 136, 2261-2282.

783 Lorenz, E. N., 1969: The predictability of a flow which possesses many scales of motion. Tellus, 21, 289-307.
784 Mass, C. F., D. Ovens, K. Westrick, and B. A. Colle, 2002: DOES INCREASING HORIZONTAL RESOLUTION PRODUCE
785 MORE SKILLFUL FORECASTS? Bull. Am. Meteorol. Soc., 83, 407-430.
786 Mitchell, K., 2005: The community Noah land-surface model (LSM), 7.
787 Nielsen, E. R., and R. S. Schumacher, 2016: Using Convection-Allowing Ensembles to Understand the Predictability
788 of an Extreme Rainfall Event. Mon. Wea. Rev., 144, 3651-3676.
789 Reynolds, R. W., N. A. Rayner, T. M. Smith, D. C. Stokes, and W. Wang, 2002: An Improved In Situ and Satellite SST
790 Analysis for Climate. J. Climate, 15, 1609-1625.
791 Savijarvi, H., 1991: The United States Great Plains diurnal ABL variation and the nocturnal low-level jet. Mon. Wea.
792 Rev., 119, 833-840.
793 Schaefer, J. T., 1986: The dryline. Mesoscale Meteorology and Forecasting, P. Ray, Ed., Amer. Meteor. Soc., 549-570.
794 Selz, T., and G. C. Craig, 2015: Upscale Error Growth in a High-Resolution Simulation of a Summertime Weather Event
795 over Europe. Mon. Wea. Rev., 143, 813-827.
796 Skamarock, W. C., J. B. Klemp, J. Dudhia, D. O. Gill, D. M. Barker, W. Wang, and J. G. Powers, 2008: A description of
797 the Advanced Research WRF version 3. NCAR Technical note-475+ STR.
798 Skinner, P. S., and Coauthors, 2020: The impact of radar assimilation on short-term and next-day thunderstorm
799 forecasts in the 2016 Community Leveraged Unified Ensemble (CLUE). Mon. Wea. Rev., Conditionally accepted.
800 Sun, X., M. Xue, J. Brotzge, R. McPherson, X. Hu, and X.-Q. Yang, 2016: An evaluation of dynamic downscaling of
801 central plains summer precipitation using a WRF-based regional climate model at a convection-permitting 4-
802 km resolution. J. Geophy. Res., 121, 13801-13826.
803 Sun, Y. Q., and F. Zhang, 2016: Intrinsic versus Practical Limits of Atmospheric Predictability and the Significance of
804 the Butterfly Effect. J. Atmos. Sci., 73, 1419-1438.
805 Surcel, M., M. Berenguer, and I. Zawadzki, 2010: The Diurnal Cycle of Precipitation from Continental Radar Mosaics
806 and Numerical Weather Prediction Models. Part I: Methodology and Seasonal Comparison. Mon. Wea. Rev.,
807 138, 3084-3106.
808 Surcel, M., I. Zawadzki, and M. K. Yau, 2014: A Study on the Scale Dependence of the Predictability of Precipitation
809 Patterns. J. Atmos. Sci., 72, 216-235.
810 ——, 2015: The Case-to-Case Variability of the Predictability of Precipitation by a Storm-Scale Ensemble Forecasting
811 System. Mon. Wea. Rev., 144, 193-212.

812 Surcel, M., I. Zawadzki, M. K. Yau, M. Xue, and F. Kong, 2017: More on the Scale Dependence of the Predictability of
813 Precipitation Patterns: Extension to the 2009–13 CAPS Spring Experiment Ensemble Forecasts. Mon. Wea. Rev.,
814 145, 3625-3646.
815 Tan, Z.-M., F. Zhang, R. Rotunno, and C. Snyder, 2004: Mesoscale Predictability of Moist Baroclinic Waves:
816 Experiments with Parameterized Convection. J. Atmos. Sci., 61, 1794-1804.
817 Thompson, G., P. R. Field, R. M. Rasmussen, and W. D. Hall, 2008: Explicit Forecasts of Winter Precipitation Using an
818 Improved Bulk Microphysics Scheme. Part II: Implementation of a New Snow Parameterization. Mon. Wea. Rev.,
819 136, 5095-5115.
820 Trier, S. B., J. W. Wilson, D. A. Ahijevych, and R. A. Sobash, 2017: Mesoscale Vertical Motions near Nocturnal
821 Convection Initiation in PECAN. Monthly Weather Review, 145, 2919-2941.
822 Trier, S. B., C. A. Davis, D. A. Ahijevych, M. L. Weisman, and G. H. Bryan, 2006: Mechanisms Supporting Long-Lived
823 Episodes of Propagating Nocturnal Convection within a 7-Day WRF Model Simulation. J. Atmos. Sci., 63, 2437-
824 2461.
825 Walser, A., D. Lüthi, and C. Schär, 2004: Predictability of Precipitation in a Cloud-Resolving Model. Mon. Wea. Rev.,
826 132, 560-577.
827 Wapler, K., F. Harnisch, T. Pardowitz, and F. Senf, 2015: Characterisation and predictability of a strong and a weak
828 forcing severe convective event – a multi-data approach. Meteorologische Zeitschrift, 24, 393-410.
829 Weyn, J. A., and D. R. Durran, 2017: The Dependence of the Predictability of Mesoscale Convective Systems on the
830 Horizontal Scale and Amplitude of Initial Errors in Idealized Simulations. J. Atmos. Sci., 74, 2191-2210.
831 ——, 2018: Ensemble Spread Grows More Rapidly in Higher-Resolution Simulations of Deep Convection. J. Atmos.
832 Sci., 75, 3331-3345.
833 ——, 2019: The scale dependence of initial-condition sensitivities in simulations of convective systems over the
834 southeastern United States. Quart. J. Roy. Meteor. Soc., 145, 57-74.
835 Wu, N., X. Zhuang, J. Min, and Z. Meng, 2020: Practical and Intrinsic Predictability of a Warm-Sector Torrential Rainfall
836 Event in the South China Monsoon Region. J. Geophys. Res. D: Atmos., 125, e2019JD031313.
837 Xue, M., and W. J. Martin, 2006: A high-resolution modeling study of the 24 May 2002 dryline case during IHOP. Part
838 II: Horizontal convective rolls and convective initiation. Mon. Wea. Rev., 134, 172–191.
839 Xue, M., D.-H. Wang, J.-D. Gao, K. Brewster, and K. K. Droegemeier, 2003: The Advanced Regional Prediction System
840 (ARPS), storm-scale numerical weather prediction and data assimilation. Meteor. Atmos. Phy., 82, 139-170.

841 Xue, M., X. Luo, K. Zhu, Z. Sun, and J. Fei, 2018: The Controlling Role of Boundary Layer Inertial Oscillations in Meiyu
842 Frontal Precipitation and Its Diurnal Cycles Over China. J. Geophys. Res. D: Atmos., 123, 5090-5115.
843 Xue, M., and Coauthors, 2007: CAPS realtime storm-scale ensemble and high-resolution forecasts as part of the
844 NOAA Hazardous Weather Testbed 2007 spring experiment. 22nd Conf. Wea. Anal. Forecasting/18th Conf. Num.
845 Wea. Pred., Amer. Meteor. Soc., CDROM 3B.1.
846 Zhang, F., C. Snyder, and R. Rotunno, 2003: Effects of Moist Convection on Mesoscale Predictability. J. Atmos. Sci.,
847 60, 1173-1185.
848 Zhang, F., N. Bei, R. Rotunno, C. Snyder, and C. C. Epifanio, 2007: Mesoscale Predictability of Moist Baroclinic Waves:
849 Convection-Permitting Experiments and Multistage Error Growth Dynamics. J. Atmos. Sci., 64, 3579-3594.
850 Zhang, X., 2019: Multiscale Characteristics of Different-Source Perturbations and Their Interactions for Convection-
851 Permitting Ensemble Forecasting during SCMREX. Mon. Wea. Rev., 147, 291-310.
852 Zhuang, X., J. Min, L. Zhang, S. Wang, N. Wu, and H. Zhu, 2020: Insights into Convective-scale Predictability in East
853 China: Error Growth Dynamics and Associated Impact on Precipitation of Warm-Season Convective Events. Adv.
854 Atmos. Sci., 37, 893-911.
855 Zimmer, M., G. C. Craig, C. Keil, and H. Wernli, 2011: Classification of precipitation events with a convective response
856 timescale and their forecasting characteristics. Geophys. Res. Lett., 38.
857

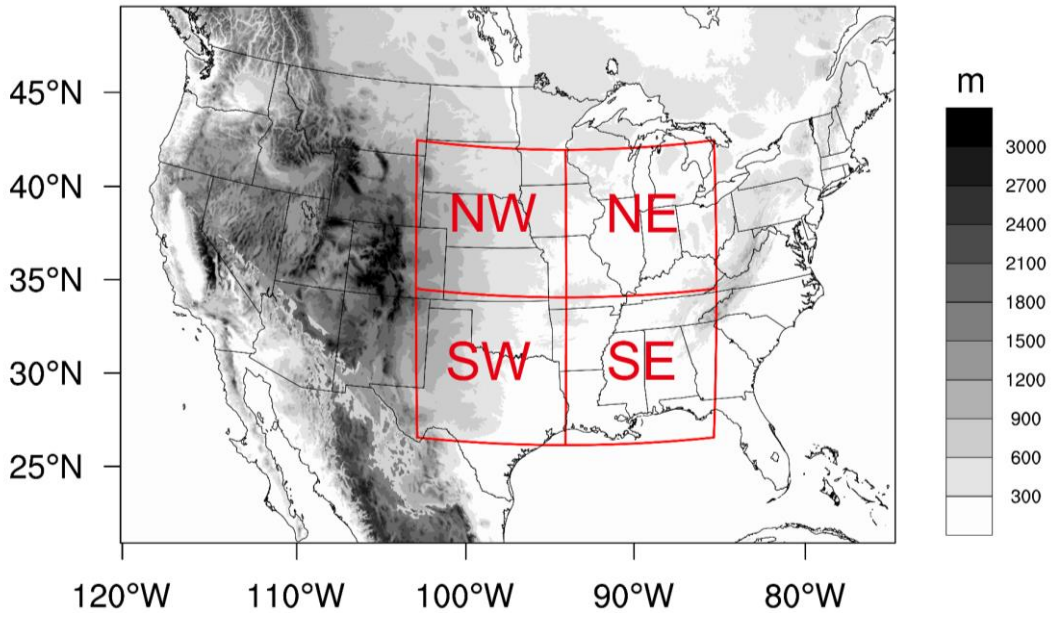

858

859 Fig. 1. The forecast model domain with terrain height in shading. The red
860 rectangle corresponds to the analysis domain that is divided into four
861 equal-sized quadrants or subregions used in our analyses.
862

863

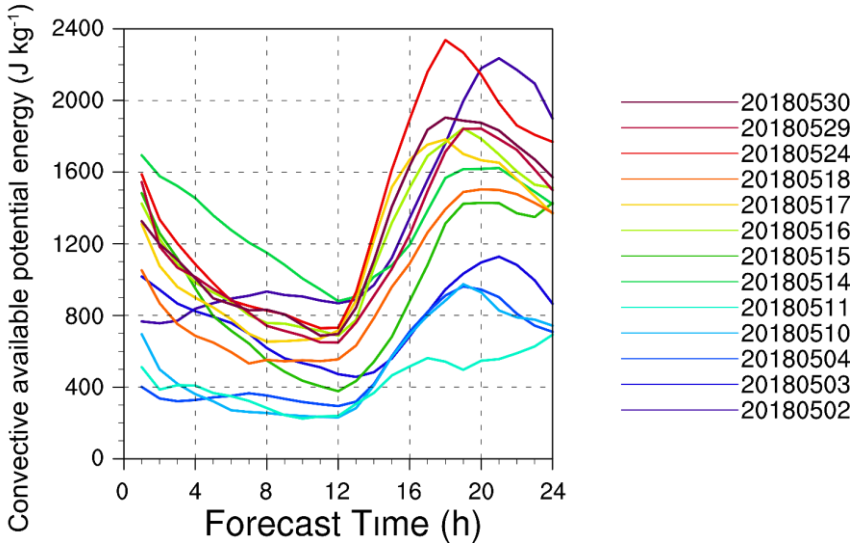

864

865 Fig. 2. The convective available potential energy (CAPE) averaged over
866 the entire analysis domain with rainfall higher than 0.5 mm h^{-1} as a
867 function of forecast lead time for each case indicated in the legend.

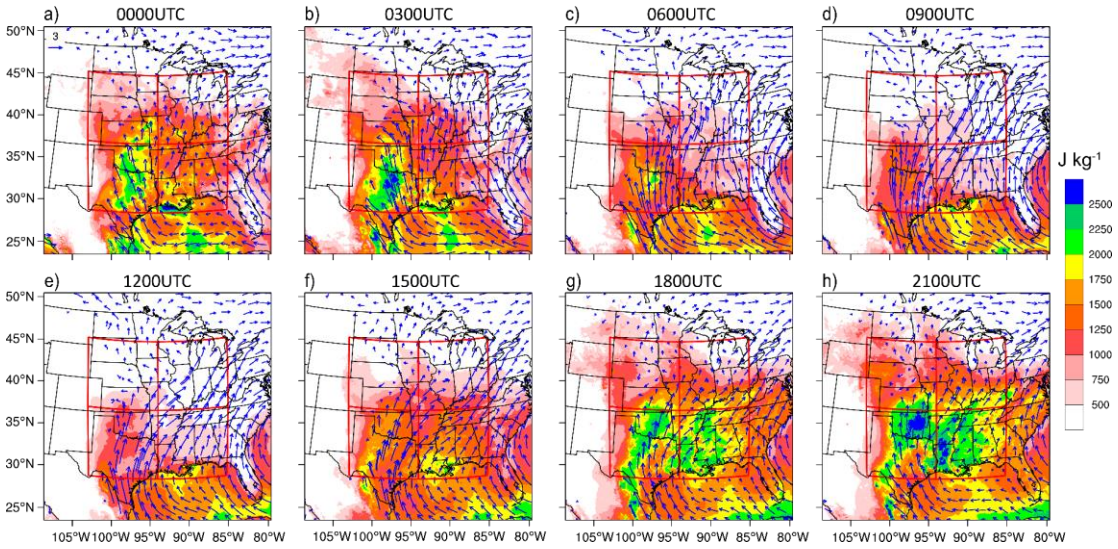

868

869 Fig. 3. Ensemble mean CAPE (shaded) and 925-hPa horizontal wind
870 vectors, from (a) 0000 UTC (h) through 2100 UTC (h), every 3 h averaged
871 over all 14 cases.
872

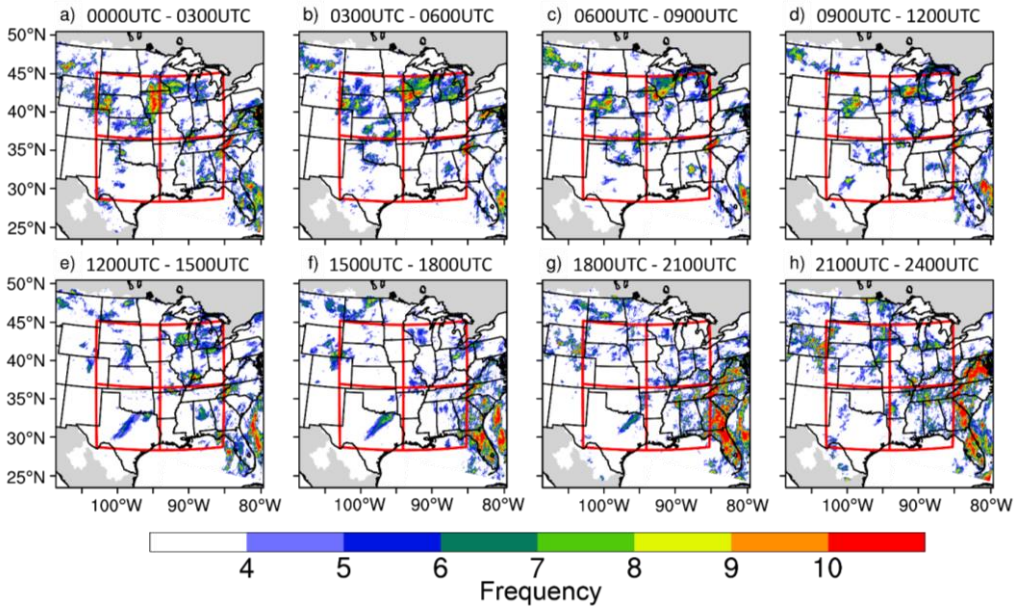

873

874 Fig. 4. Spatial distribution of 3 h accumulated precipitation frequency
875 maps with precipitation rate exceeding 0.5 mm h^{-1} at different ending
876 times: (a) 0300 UTC, (b) 0600 UTC, (c) 0900 UTC, (d) 1200 UTC, (e) 1500
877 UTC, (f) 1800 UTC, (g) 2100 UTC, (h) 2400 UTC.

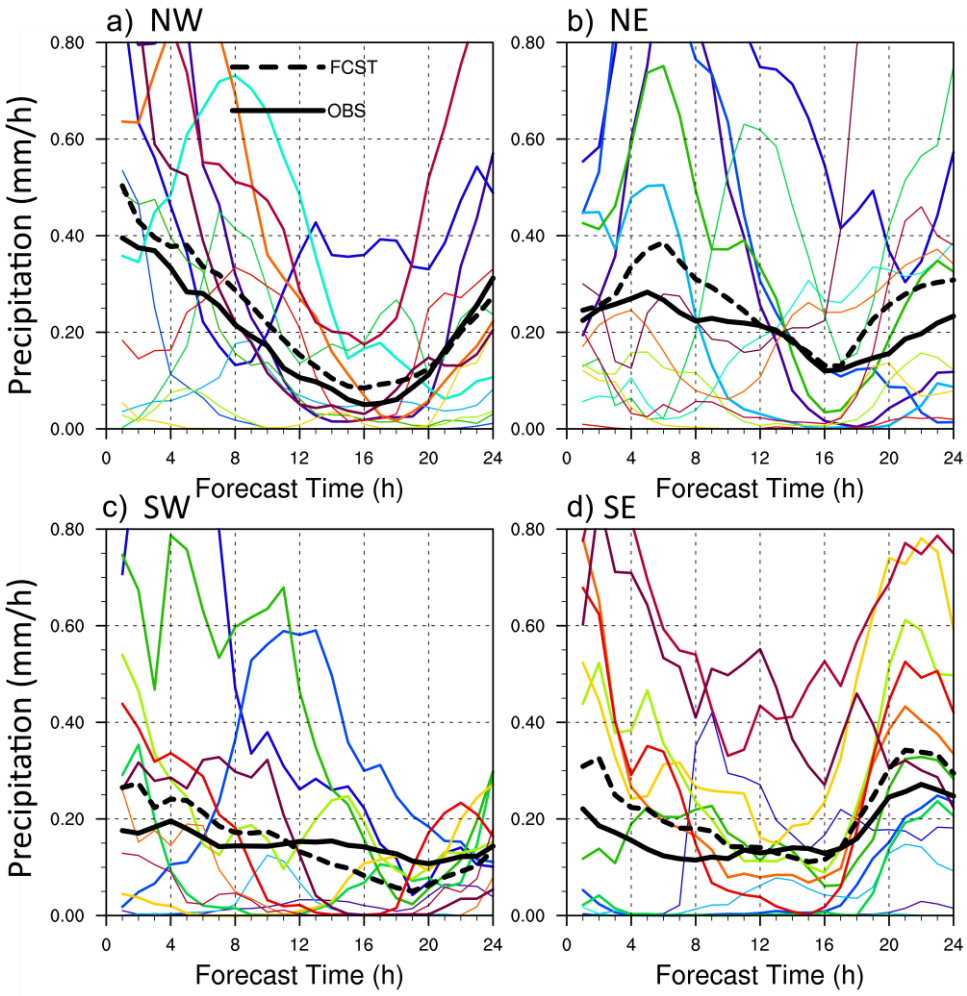

878

879 Fig. 5. Time evolution of region-averaged forecast and observed precipitation for
880 the (a) NW, (b) NE, (c) SW, (d) SE subregions. The color solid lines are for the
881 individual cases for each subregion (with the color legend shown in Fig. 2), and
882 black dashed line for the average of all cases and solid line is for observation.
883

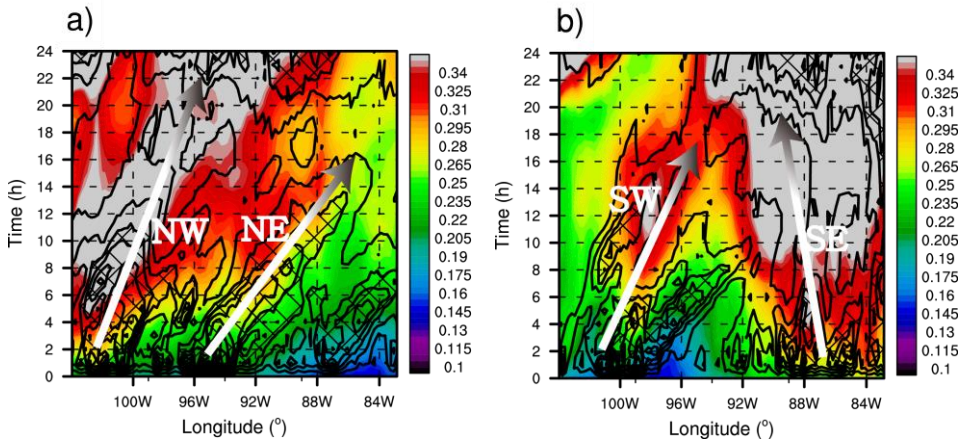

884

885 Fig. 6. Hovmoller diagrams (latitudinal averaged, time-longitude) for NRMDTE
886 (shaded) and precipitation (contours) for (a) the northern subdomains and (b)
887 southern subdomains, averaged over all 14 cases.
888

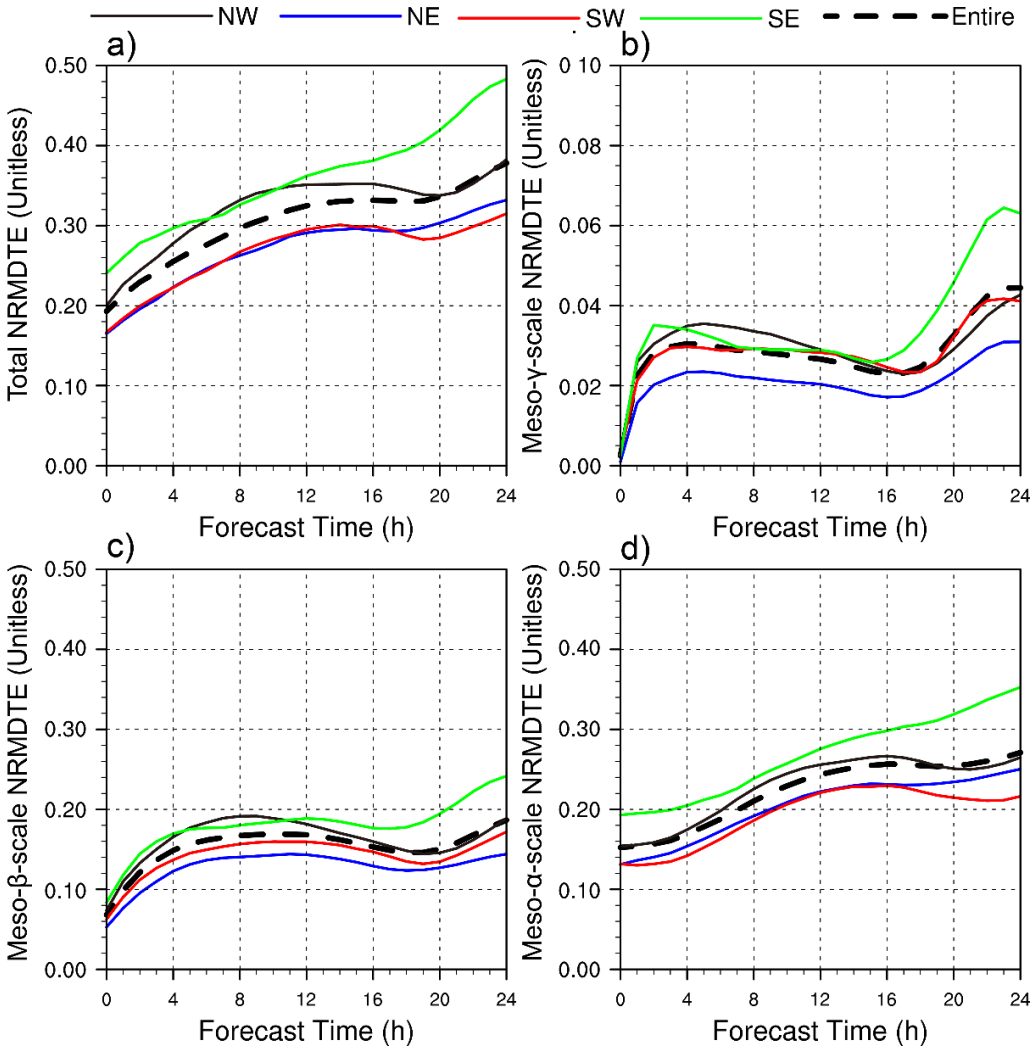

889

890 Fig. 7. Time evolution of NRMDTE at different scales: (a) Total, (b) Meso-γ, (c)
891 Meso-β, and (d) Meso-α, for the entire (black) and 4 subregions (color lines).

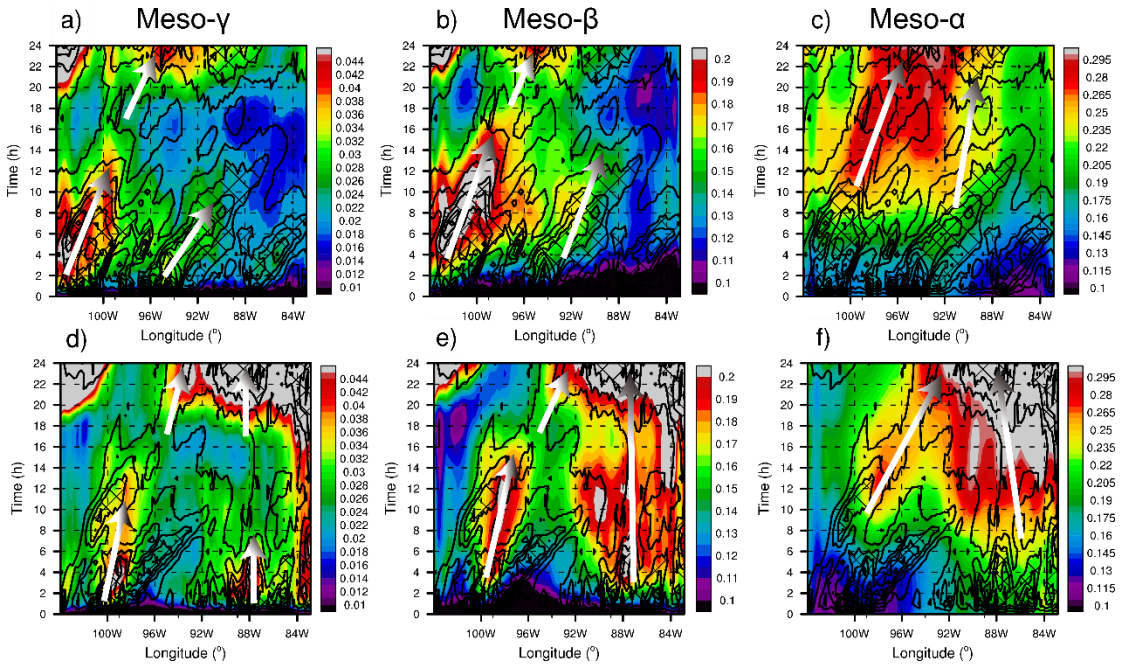

Fig. 8. Hovmoller diagrams (latitudinal averaged, time-longitude) for the case-averaged NRMDTE (color) at different scales and precipitation (contours), (a, d) Meso-γ; (b, e) Meso-β; (c, f) Meso-α for the northern (upper row) and southern regions (lower row). The ordinate indicates the forecast hour starting from 0000 UTC.

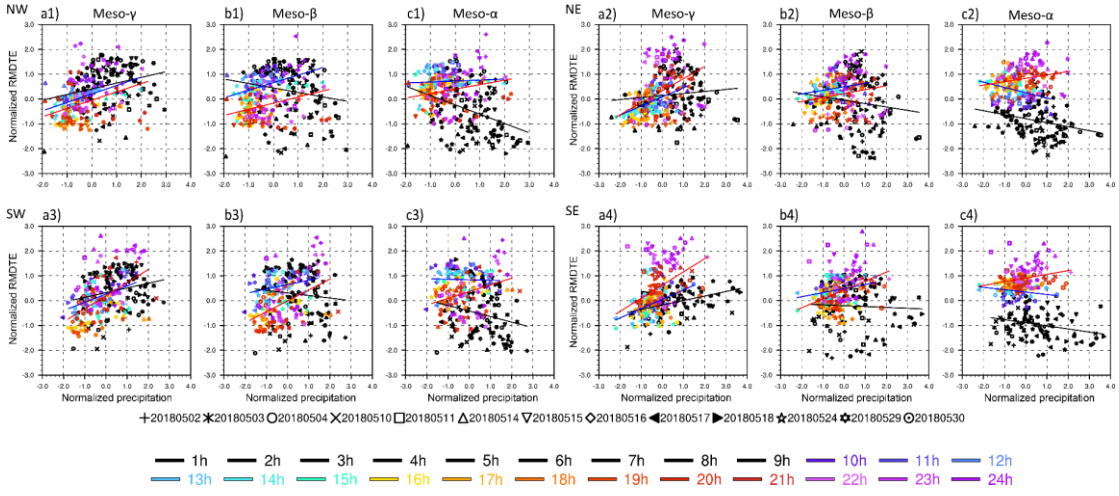

Fig. 9. Scatterplots of the normalized RMDTE at different scales (a) Meso-γ, (b) Meso-β, (c) Meso-α vs normalized precipitation (>0.5 mm /h^{-1}) at different lead times (see legend for corresponding colors).

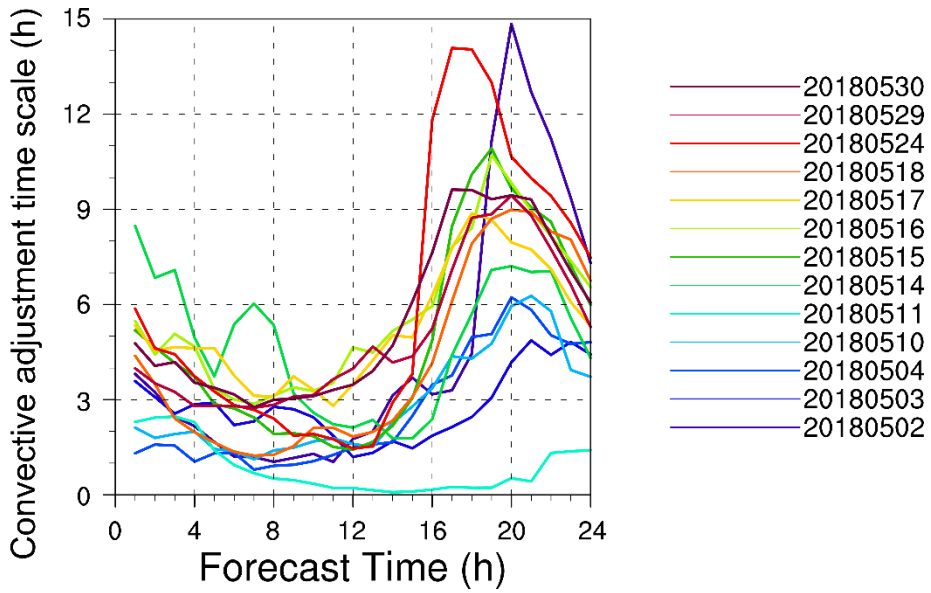

905

906 Fig. 10. The convective adjustment time scale (τ_c) averaged over the
907 entire analysis domain with rainfall higher than 0.5 mm h^{-1} as a function
908 of forecast lead time for each case indicated in the legend.
909

910

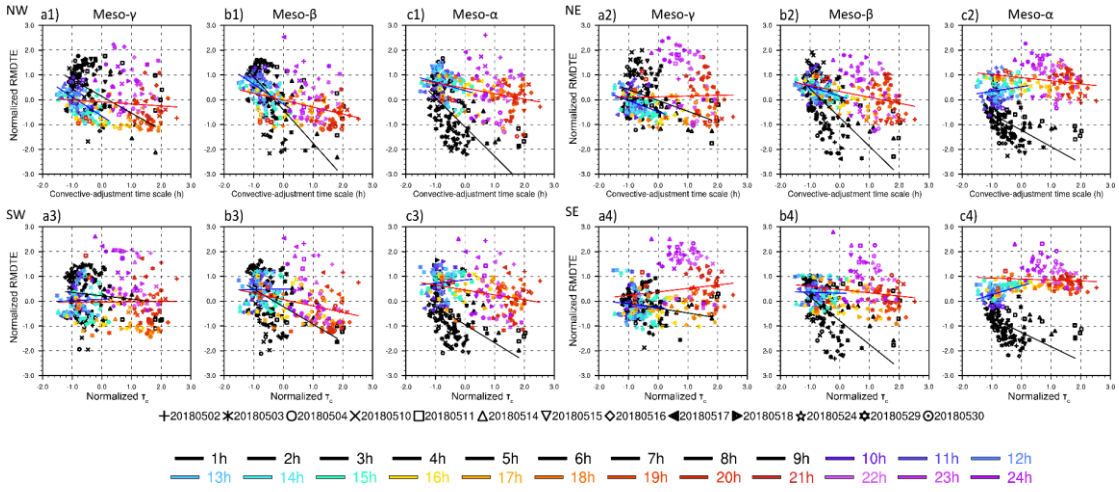

911

912 Fig. 11. Same as Fig. 9, but for normalized RMDTE vs normalized
913 convective adjustment timescale (τ_c).
914

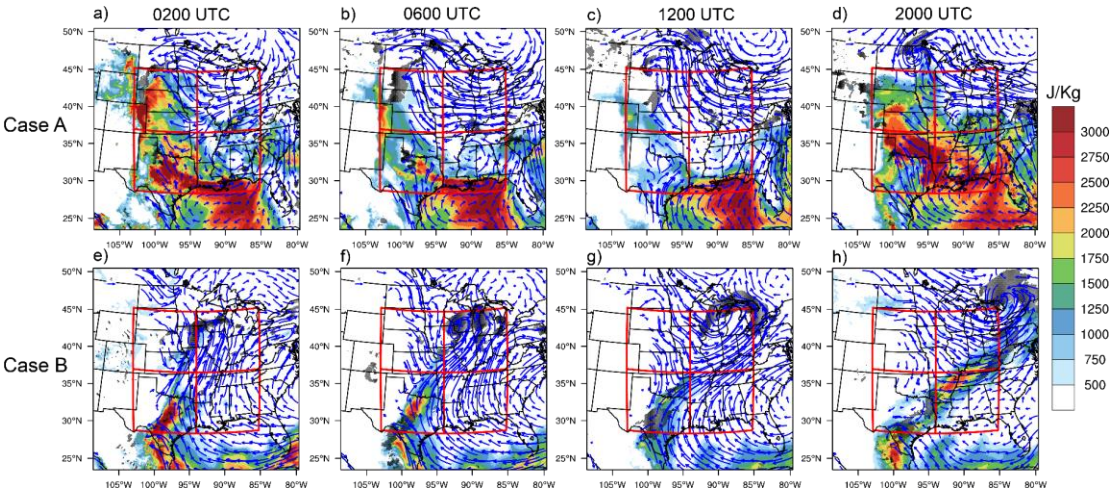

Fig. 12. Ensemble mean most unstable CAPE (MUCAPE, shaded), 925-hPa horizontal wind vectors and precipitation rate (dotted shading) for Case A (top row) and Case B (bottom row) at different valid times: (a, e) 0200 UTC, (b, f) 0600 UTC, (c, e) 1200UTC, (d, h) 2000 UTC.

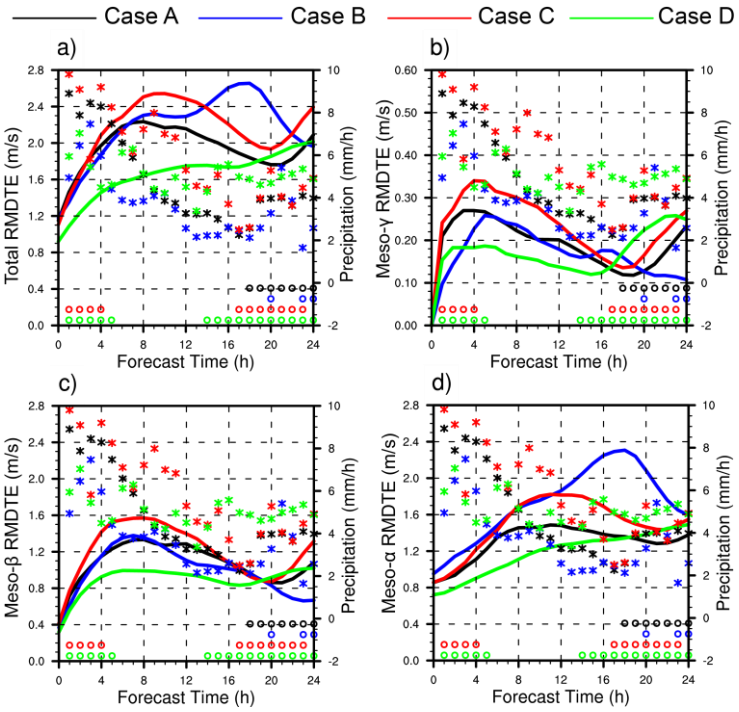

Fig. 13. Time evolution of RMDTEs (solid curves) for four selected cases averaged in the corresponding regions at different scales: (a) Total, (b) Meso-γ, (c) Meso-β, (d) Meso-α, the stars indicate area-averaged precipitation exceeding 0.5 mm h^{-1}, and the circles are indicators of weakly forcing (defined in section 5b) at certain times. The cases are color coded.

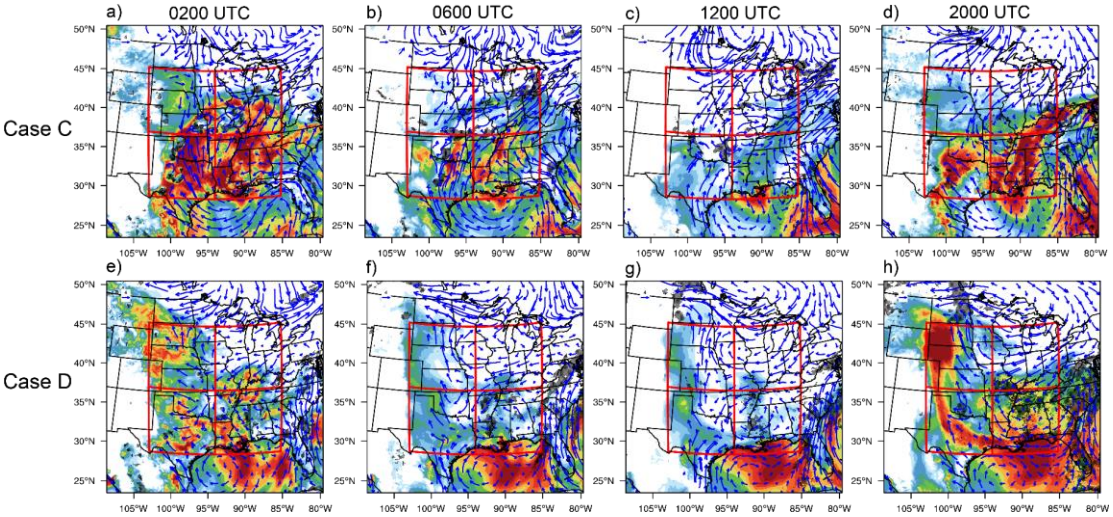

Fig. 14. Ensemble mean most unstable CAPE (MUCAPE, shaded), 925-hPa horizontal wind vectors and precipitation rate (dotted shading) for Case C (top row) and Case D (bottom row) at different valid times: (a, e) 0200 UTC, (b, f) 0600 UTC, (c, e) 1200UTC, (d, h) 2000 UTC.